



Cite as
Nano-Micro Lett.
(2025) 17:165

Received: 21 November 2024
Accepted: 24 January 2025
© The Author(s) 2025

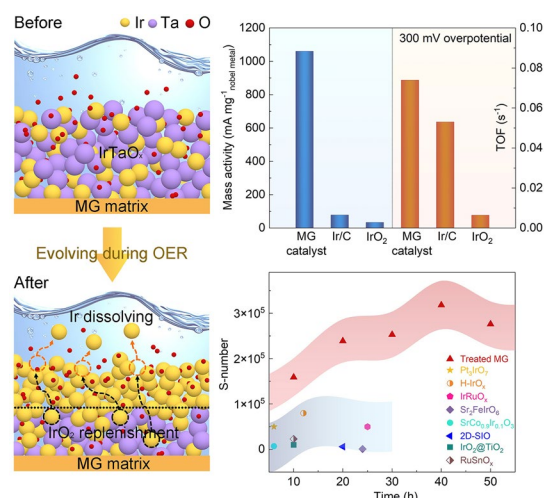
Durable Acidic Oxygen Evolution Via Self-Construction of Iridium Oxide/Iridium-Tantalum Oxide Bi-Layer Nanostructure with Dynamic Replenishment of Active Sites

Qi Guo¹, Rui Li¹ ✉, Yanan Zhang¹, Qiqin Zhang¹, Yi He¹, Zhibin Li², Weihong Liu³, Xiongjun Liu² ✉, Zhaoping Lu² ✉

HIGHLIGHTS

- A self-constructed catalyst with in situ formed IrO₂/IrTaO_x bi-layer nanostructure was fabricated for high-efficiency acidic oxygen evolution reaction by using an Ir–Ta-based metallic glass as the matrix.
- The coordinated nature of the catalyst's active site is manipulated through electronic interaction between Ir and Ta, resulting in superior activity and stability.
- The underlying amorphous IrTaO_x layer dynamically replenishes the depletion of surface Ir sites through inward crystallization and selective dissolution to ensure long-term durability.

ABSTRACT Proton exchange membrane (PEM) water electrolysis presents considerable advantages in green hydrogen production. Nevertheless, oxygen evolution reaction (OER) catalysts in PEM water electrolysis currently encounter several pressing challenges, including high noble metal loading, low mass activity, and inadequate durability, which impede their practical application and commercialization. Here we report a self-constructed layered catalyst for acidic OER by directly using an Ir–Ta-based metallic glass as the matrix, featuring a nanoporous IrO₂ surface formed in situ on the amorphous IrTaO_x nanostructure during OER. This distinctive architecture significantly enhances the accessibility and utilization of Ir, achieving a high mass activity of 1.06 A mg_{Ir}⁻¹ at a 300 mV overpotential, 13.6 and 31.2 times greater than commercial Ir/C and IrO₂, respectively. The catalyst also exhibits superb stability under industrial-relevant current densities in acid, indicating its potential for practical uses. Our analyses reveal that the coordinated nature of the surface-active Ir species is effectively modulated through electronic interaction between Ir and Ta, preventing them from rapidly evolving into high valence states and suppressing the lattice oxygen participation. Furthermore, the underlying IrTaO_x dynamically replenishes the depletion of surface-active sites through inward crystallization and selective dissolution, thereby ensuring the catalyst's long-term durability.



KEYWORDS Self-construction; Nanoporous; Electronic interaction; Replenishment; Proton exchange membrane (PEM) water electrolysis

✉ Rui Li, ruli@nwpu.edu.cn; Xiongjun Liu, xjliu@ustb.edu.cn; Zhaoping Lu, luzp@ustb.edu.cn

¹ Institute of Clean Energy, Yangtze River Delta Research Institute, Northwestern Polytechnical University, Xi'an 710072, People's Republic of China

² Beijing Advanced Innovation Center for Materials Genome Engineering, State Key Laboratory for Advanced Metals and Materials, University of Science and Technology Beijing, Beijing 100083, People's Republic of China

³ School of Materials Science and Engineering, Harbin Institute of Technology Shenzhen, Shenzhen 518055, People's Republic of China

Published online: 25 February 2025



SHANGHAI JIAO TONG UNIVERSITY PRESS

Springer

1 Introduction

Green hydrogen produced through water electrolysis is considered a promising energy carrier for balancing the intermittency of renewable energy sources [1, 2]. Among various water electrolysis technologies, proton-exchange membrane (PEM) water electrolysis has recently garnered significant research interest due to its advantages of high current density, low resistance, and super gas purity [3–7], outperforming the dominant alkaline water electrolysis. However, the large-scale implementation of PEM water electrolysis is impeded by the scarcity of active and stable anodic oxygen evolution reaction (OER) electrocatalysts [8, 9]. Most existing OER catalysts are impaired by sluggish reaction kinetics in acidic environments and suffer from severe degradation under harsh corrosive and oxidative conditions [10–13]. To date, precious iridium (Ir)-based materials, such as IrO₂, remain the only known practical OER catalysts [14–17]. Nevertheless, they still face challenges of low mass activity and thermodynamic instability during prolonged and high-current-density acidic oxygen evolution [18, 19]. Therefore, to enhance the competitiveness of PEM water electrolysis, it is highly desirable, yet remains a challenge, to develop novel acidic OER electrocatalysts with higher activity, long-term stability, and lower Ir content.

Recently, alloying strategies have emerged as a promising approach to enhancing acidic OER performance and reducing the content of Ir [20–22]. Various studies indicate that alloying or doping high-valence metals with strong electronegativity and high chemical stability, such as Ta, W, and Nb, can effectively enhance the OER activity and stability of Ir-based catalysts. For instance, synthesized compounds such as Ir_{0.1}Ta_{0.9}O_{2.45} [23], Ta_xTm_yIr_{1-x-y}O_{2-δ} [24], Ir-W@Ir-WO_{3-x} [25], and Ir/Nb₂O_{5-x} [26] demonstrate superior OER activity and stability compared to basic IrO₂ nanoparticles in acid media due to the electronic structure manipulation induced by high-valence metals, which can effectively optimize the Ir–O bonding strength and thereby enhancing the OER electrocatalysis. However, the stability of these nanocatalysts is still limited under a low current density (e.g., 10 mA cm⁻²) due to their inevitable agglomeration, dissolution, or detachment from the support (usually the carbon) at higher current densities, which can lead to a significant decline in OER performance [27–29]. Indeed, the dissolution of active Ir species is unavoidable during acidic

OER, and this issue becomes more severe under industrial current densities [30–32]. Therefore, it is highly desirable to identify an appropriate balance that can mitigate unwanted decomposition while facilitating rapid electron transfer.

To this end, herein we report a self-constructed IrO₂/IrTaO_x bi-layer nanostructure as an efficient catalyst for acidic OER by utilizing an Ir–Ta–Ni–Nb metallic glass (MG) as the matrix. The IrTaO_x nanostructure with in situ formed catalytically active IrO₂ nanoporous surface exhibits an ultralow overpotential of 211 mV (218 mV, experimental corrected) at 10 mA cm⁻² and high mass activity of 1.06 A mg_{Ir}⁻¹ at 300 mV overpotential. Additionally, the catalyst demonstrates enhanced stability for over 650 h with negligible activity decay under a current density of 100 mA cm⁻². The exceptional acidic OER performance outperforms that of commercial Ir/C and IrO₂, as well as many state-of-the-art precious nanocatalysts. Experimental analyses and density functional theory (DFT) calculations reveal that the strong electronic interactions between Ir and Ta effectively modulate the coordination nature of surface Ir active sites, which will prevent them from rapidly evolving to a higher valence state and dissolving. Furthermore, the underlying amorphous IrTaO_x is dynamically evolving into IrO₂ nanocrystals to continuously replenish the surface catalytically active sites in the event of their dissolution during prolonged acidic OER operations, thereby promoting the durability and maintaining the activity of the catalyst. This work proposes an innovative strategy for designing highly efficient and stable OER alloy catalysts for practical applications in PEM water electrolysis.

2 Experimental Section

2.1 Materials

The designed Ir–Ta-based alloy ingots with different nominal compositions were prepared by melting a mixture of high-purity (99.99 wt%) elements under a Ti-gettered argon atmosphere and remelted at least five times to ensure chemical homogeneity. Then, a melt-spinning technique was used to rapidly quench the remelted alloy ingots onto the cold surface of a spinning copper wheel to fabricate the MG ribbons with a thickness of ~30 μm and a width of ~1 mm. Acidic treatment of the MG samples was carried out in an

HF solution (0.5 M) for pre-activation and was then repeatedly ultrasonicated in deionized water and dehydrated alcohol to remove residual chemical substances.

2.2 Structural Characterizations

The phase structure of the samples was determined by X-ray diffraction (XRD, Bruker D8 Advance, Cu-K α) and grazing-incidence XRD (GIXRD, Rigaku DMAX-2500, Cu-K α) with an incident angle of 0.5°. Microstructural characterizations were conducted using scanning electron microscopy (SEM, Zeiss Gemini 460) equipped with an energy-dispersive X-ray spectrometer (EDS), transmission electron microscope (TEM, Themis Talos F200S), and scanning TEM (STEM, Themis Z) equipped with a spherical aberration corrector. The TEM specimens were prepared using a focused-ion beam (FIB, Helios G5 UX) method. X-ray photoelectron spectroscopy (XPS, Thermo Scientific Nexsa) with an Al K α (mono, 1486.68 eV) anode at an energy level of 72 W in a vacuum of 5×10^{-7} Pa was employed to probe the surface chemical state and the binding energies of the constituent elements. All binding energies were calibrated at the C 1s position (284.8 eV) from the contaminant carbon in the vacuum chamber of the instrument. The contents of various elements including Ir, Ta, Ni, and Nb were determined by an inductively coupled plasma-optical emission spectrometer (ICP-OES, PerkinElmer Avio 200).

2.3 Electrochemical Measurements

All electrochemical measurements were taken on an electrochemical workstation (ParSTAT MC) using a typical three-electrode system equipped with a carbon rod as the counter electrode and a standard Ag/AgCl (3.0 M KCl) electrode as the reference electrode at room temperature. The as-spun and acid-treated MG ribbons with a fixed size of 1 mm \times 5 mm \times 30 μ m were directly used as the working electrodes. The electrocatalytic measurements were conducted in an acidic electrolyte of 0.5 M H₂SO₄ aqueous solution. The commercial IrO₂ and Ir/C (20 wt%) catalyst inks were prepared and loaded on a glass carbon electrode (diameter: 4 mm), respectively. The mass loading of these precious catalysts was about 0.2 mg cm⁻². For convenience, all potentials in this study were converted to reversible hydrogen

electrode (RHE) by the Nernst equation of $E_{\text{RHE}} = E_{\text{Ag/AgCl}} + 0.197 + 0.0591 \times \text{pH}$ and the overpotential (η) for OER was calculated using the equation of: $\eta = E_{\text{RHE}} - 1.23$. Electrochemical impedance spectroscopy (EIS) spectra were obtained in a frequency range of 10⁵ Hz to 0.1 Hz with an amplitude of 10 mV. All linear scan voltammetry curves were conducted at a scan rate of 5 mV s⁻¹. Before each linear sweep voltammetry (LSV) test, the catalyst electrodes were measured with several cyclic voltammetry (CV) cycles until a stable CV curve was obtained. The iR correction of polarization curves was performed using the solution resistance estimated from EIS measurements. The potential was then corrected using the equation of $E_{iR\text{-corrected}} = E - iR$, where i is the current and R is the uncompensated electrolyte Ohmic resistance measured by EIS. The mass activity of the catalysts was calculated using the equation of $j_{\text{mass}} = i_{\text{geo}} / (m_{\text{act}} \times \text{Ir}_{\text{wt}\%})$, where i_{geo} is the geometric current obtained from LSV, m_{cat} is the mass of the catalytic layer, and $\text{Ir}_{\text{wt}\%}$ is the mass ratio of Ir. The turnover frequency (TOF) was calculated using the equation of $\text{TOF} = \frac{|j| \times A_{\text{geo}} \times N_A / (4F)}{\text{ECSA} / S_a}$, where j is the geometric current density, A_{geo} is the geometric area of the catalytic surface, N_A is the Avogadro constant (6.022×10^{23} mol⁻¹), F is the Faraday constant (96,485.3 C mol⁻¹), ECSA is the electrochemically active surface area of the catalyst, and S_a is the average area of each active site [33]. The ECSA was calculated using the equation of $\text{ECSA} = C_{\text{dl}} / C_s$, where C_{dl} is the electrical double-layer capacitor and is measured from double-layer charging curves using cyclic voltammograms in a non-Faradaic region with scan rates ranging from 10 to 100 mV s⁻¹. C_s is the specific capacitance of the sample (set as 40 μ F cm⁻² according to the previous reports) [34]. The chronopotentiometry tests under the different current densities ranging from 100 mA cm⁻² to 1 A cm⁻² were carried out to evaluate the long-term durability of the catalyst. ICP measurement was used to determine the dissolved elements in the electrolyte after the durability test. The S-number was calculated using the equation: $\text{S-number} = \frac{n_{\text{O}_2}}{n_{\text{Ir}}}$, where n_{Ir} is the total amount of Ir dissolved in the electrolyte, n_{O_2} is the amount of oxygen molecules produced during a 650-h test at 100 mA cm⁻². This value was calculated according to Faraday's laws of electrolysis of $n_{\text{O}_2} = \frac{j \times s \times t}{z \times F}$, where j is the geometric current density, s is the geometry area of the electrode, t is the electrolysis time, z is the number of electrons

transferred to produce an oxygen molecule, and F is the Faraday constant.

Isotope-labeled differential electrochemical mass spectrometry (DEMS) measurements were taken in an electrochemical cell with a typical three-electrode system equipped with an operando DEMS system (QAS-100, Linglu Instruments), where the MG catalyst samples with ^{18}O -labeling were used as the working electrodes, an Ag/AgCl electrode prefilled with saturated KCl aqueous solution was used as the reference electrode, and a Pt plate was used as the counter electrode. CV measurement was taken in ^{16}O 0.5 M H_2SO_4 electrolyte with a scan rate of 5 mV s^{-1} . The gaseous products including $^{32}\text{O}_2$, $^{34}\text{O}_2$, and $^{36}\text{O}_2$ were probed in real time by the mass spectrometer.

2.4 Theoretical Calculation

All calculations were carried out in the framework of DFT using the Vienna Ab initio Simulation Package (VASP) [35–37]. The generalized gradient approximation (GGA) with the Perdew–Burke–Ernzerhof (PBE) function was used to describe the exchange–correlation energy [38]. The projected augmented wave (PAW) method and pseudopotentials were used to describe the interactions between valence electrons and ions [39]. To ensure the efficiency of the computational results and parallel computing, a $2 \times 2 \times 3$ k-point grid under Monkhorst–Pack with a truncation energy of 450 eV is used in the optimization process. To correct the localization effect of D-orbital electrons in transition metal atoms, the value of efficient Hubbard U was set as 3.0 eV for both Ir and Ta. The lattice parameters and ionic positions of all crystals were fully relaxed, and the convergence criteria for the total energy of all relaxed atoms and the final force were 10^{-5} eV and 0.03 eV \AA^{-1} , respectively.

3 Results and Discussion

3.1 Catalyst Fabrication and Acidic OER Performance

$\text{Ir}_{30}\text{Ta}_{35}\text{Ni}_{29}\text{Nb}_6$ MG matrix was prepared using a melt-spinning method. XRD pattern reveals the absence of any crystalline phase (Fig. S1), confirming the amorphous nature of the as-spun $\text{Ir}_{30}\text{Ta}_{35}\text{Ni}_{29}\text{Nb}_6$ MG precursor. Subsequently, an acid treatment was performed to create a catalytically active surface on the MG matrix. It is noted that the pre-activation

process is crucial for enhancing the electrochemical activity without compromising the amorphous structure and mechanical flexibility of the MG matrix (Fig. S2). The electrocatalytic OER performances of the as-spun MG precursor and acid-treated MG were then evaluated in a 0.5 M H_2SO_4 electrolyte and compared with commercial Ir/C and IrO_2 . In Fig. 1a, the LSV curves demonstrate that the acid-treated MG achieves an overpotential of 211 mV at a current density of 10 mA cm^{-2} (the current normalized to geometric surface area), significantly lower than that of its initial counterpart (901 mV) and the commercial catalysts (312 mV for Ir/C and 330 mV for IrO_2 , respectively). To obtain a more accurate overpotential, we adjusted the value using experimental corrections [40] (Fig. S3). The correction results indicate that the overpotential of the MG catalyst is 218 mV, with only minor fluctuations compared to the theoretical overpotential of 211 mV. The corresponding lowest Tafel slope of 37.5 mV dec^{-1} in Fig. 1b further demonstrates the superior electrochemical kinetics of the acid-treated MG. In addition, these characteristic values were compared with various Ir-based OER electrocatalysts recently reported (Fig. 1c and Table S1). Encouragingly, compared to many state-of-the-art precious nanocatalysts, the MG catalyst exhibits superior acidic OER activity. We then estimated TOF of these catalysts, which represents the number of oxygen molecules evolved per second from each active site at a specific overpotential [41]. As illustrated in Fig. 1d, the TOF value of the MG catalyst at an overpotential of 300 mV is higher than that of commercial Ir/C and IrO_2 , demonstrating the superior intrinsic activity of the catalytic Ir sites. Additionally, the faster charge transfer kinetics measured by EIS (Fig. S4) and the higher specific activity normalized by ECSA (Figs. S5 and S6) further validate the intrinsically improved OER activity of the acid-treated MG. More specifically, as a self-supporting material, the catalyst surface delivers a remarkable mass activity of $1.06\text{ A mg}_{\text{Ir}}^{-1}$ at an overpotential of 300 mV, which is 13.6 and 31.2 times relative to that of commercial Ir/C ($78.7\text{ mA mg}_{\text{Ir}}^{-1}$) and IrO_2 ($34.3\text{ mA mg}_{\text{Ir}}^{-1}$), respectively (Fig. 1d). This value also exceeds that of most Ir-based nanoparticle catalysts (Table S2), demonstrating that the MG catalyst not only possesses enhanced OER activity but also offers a cost advantage by reducing the amount of Ir usage.

In addition to high electrocatalytic activity, the operational stability of the catalyst is also a crucial metric for PEM water electrolysis. The OER durability of the MG catalyst in acid

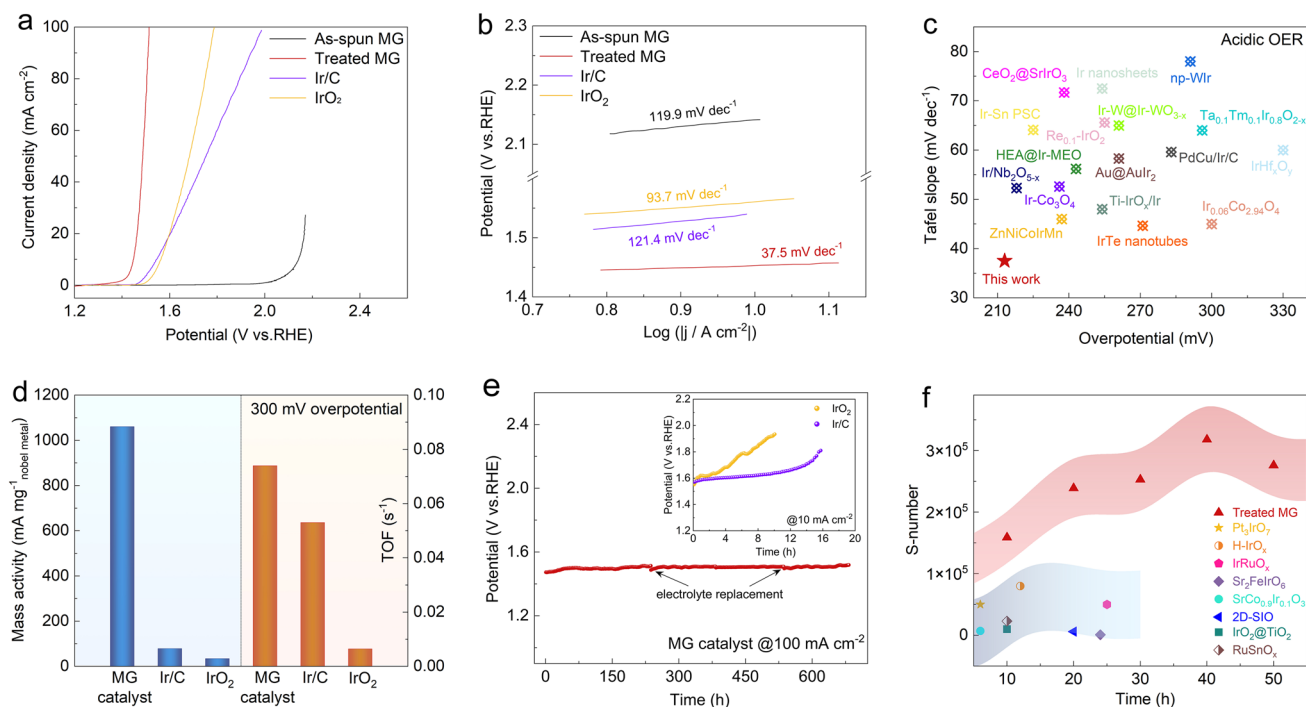


Fig. 1 Electrochemical OER performance in acid. **a** Linear polarization curves of as-spun $\text{Ir}_{30}\text{Ta}_{35}\text{Ni}_{29}\text{Nb}_6$ MG, acid-treated $\text{Ir}_{30}\text{Ta}_{35}\text{Ni}_{29}\text{Nb}_6$ MG, commercial IrO_2 , and Ir/C in a 0.5 M H_2SO_4 electrolyte. **b** The corresponding Tafel slopes. **c** Comparison of overpotential at 10 mA cm^{-2} and Tafel slope with recently reported Ir-based OER electrocatalysts in acid. **d** Mass activity and TOF of the $\text{Ir}_{30}\text{Ta}_{35}\text{Ni}_{29}\text{Nb}_6$ MG catalyst and commercial Ir/C and IrO_2 at a 300 mV overpotential. **e** Chronopotentiometry curve of the MG catalyst at a current density of 100 mA cm^{-2} . The inset shows the stability test results for the commercial Ir/C and IrO_2 catalysts at a current density of 10 mA cm^{-2} . **f** Comparison of calculated S-number of the MG catalyst with various recently reported electrocatalysts during 50-h OER stability test

was assessed using a chronopotentiometry test at a constant current density of 100 mA cm^{-2} . As illustrated in Fig. 1e, the catalyst demonstrates negligible performance degradation for over 650 h, with an overpotential degradation rate of approximately $10 \mu\text{V h}^{-1}$, which is lower than the latest specification ($14 \mu\text{V h}^{-1}$) for the PEM water electrolyzer. Notably, there is an increase in voltage of approximately 15 mV during the first 30 h of OER. This slight elevation can be attributed to the unstable electrochemical environment during the initial stages of the electrolysis system. The superior stability of the MG catalyst during the long-term stability test was further validated by the comparable LSV curves obtained after 200 and 650 h of OER (Figs. S7 and S8). In contrast, the commercial IrO_2 and Ir/C catalysts exhibit rapid increases in overpotential (approximately 10 and 16 h at 10 mA cm^{-2} , respectively) due to catalyst detachment resulting from dissolution (see inset in Fig. 1e). Furthermore, the concentration of dissolved metal ions in the electrolyte was detected by ICP-OES (Fig. S9). This measurement indicates that, although the dissolution of Ir

is inevitable under acidic OER conditions, the dissolution rate of Ir ($0.125 \mu\text{g h}^{-1}$) in the MG catalyst is much lower than that of commercial IrO_2 and Ir/C . These results strongly demonstrate the excellent acidic OER stability of the catalyst. Additionally, we employed a stability parameter known as the stability number (i.e., the S-number) to evaluate the chemical stability of the catalyst, which is defined as the ratio between the number of oxygen molecules and the number of dissolved Ir cations [42]. As illustrated in Fig. 1f, the S-number of the MG catalyst was calculated to be as high as 2.7×10^5 at the initial state ($\leq 50 \text{ h}$), which is superior to many recently reported Ir-based electrocatalysts [19, 43–49], such as $\text{IrO}_2@ \text{TiO}_2$ nanoparticles (1.0×10^4), $\text{SrCo}_{0.9}\text{Ir}_{0.1}\text{O}_3$ (7.0×10^3), and 2D-SIO (6.0×10^3). Furthermore, even after the extended durability test (i.e., 650 h), the S-number value remains high (5.4×10^4 to 9.0×10^4) (Fig. S10). This measurement indicates that the catalytic structure is stable during the long-term acidic OER operation. It is also noteworthy that even at an ampere-level current density of 1 A cm^{-2} , the overpotential of the catalyst remains as low as approximately

450 mV for more than 100 h (Fig. S11). Furthermore, under industrial conditions of 2 A cm^{-2} at 80°C , the MG catalyst maintains high stability without significant performance degradation during OER, and its S-number was calculated to be as high as 1.16×10^4 (Fig. S12). The outstanding OER performances under these industrial-relevant conditions further highlight its enormous potential for practical applications in PEM water electrolysis.

3.2 Structural Origins for the Enhanced OER Activity and Stability

As previously mentioned, the MG catalyst demonstrates exceptional acidic OER activity and stability. This raises an intriguing question regarding whether any components of the acid-treated MG structure contribute to enhancing the electrocatalytic activity and stability. To address this issue, comprehensive structural characterizations of the catalyst were performed. Figure 2a presents the cross-sectional TEM image of the acid-treated MG, which reveals an etched layer with a thickness of approximately 100 nm formed on the $\text{Ir}_{30}\text{Ta}_{35}\text{Ni}_{29}\text{Nb}_6$ MG matrix after acidic treatment. The high-resolution TEM (HRTEM) in Fig. 2b, along with the corresponding selected area electron diffraction (SAED) pattern (the inset in Fig. 2b), demonstrates an amorphous nature of the etched layer, consistent with the grazing incident XRD characterization (Fig. 2c). The TEM-EDS profile shows that the surface Ni and Nb elements were selectively etched away, resulting in the formation of an IrTaO_x -layered nanostructure (Fig. 2d). Notably, a small number of Ir-Ta-based nanocrystals was also observed within the amorphous structure (Fig. S13). This phenomenon occurs because surface corrosion under strongly acidic oxidation conditions may lead to the partial transformation of the metastable amorphous structure into a crystalline state. Moreover, it is seen that a compact passivated Ta_2O_5 crystalline layer with a thickness of approximately 15 nm formed on the surface of the amorphous IrTaO_x layer. From the perspective of reaction kinetics, the corrosion mechanism of the as-spun MG in HF can be described as a diffusion process between metal elements and the medium in the HF solution (i.e., F^- , O^{2-} , and OH^-) [50]. The catalytically active IrTaO_x nanostructure forms on the MG matrix due to the preferential etching of Ni and Nb by F^- and the oxidation of Ir and Ta by O^{2-} , resulting in improved OER activity and a 4-day-acid-treated

MG yields the best performance (Figs. S14 and S15). As the treatment time is further extended, elemental Ta readily reacts with O^{2-} and OH^- to generate a passivation layer on the surface [51–53]. The gradually formed Ta_2O_5 passivation layer protects the IrTaO_x layer and the MG matrix from excessive corrosion, thereby stabilizing the layered catalyst structure. The STEM elemental mapping analyses (Fig. 2e) further confirm the formation of the composite oxide layers on the MG matrix and the elemental distributions.

We assume that the amorphous IrTaO_x nanostructure is the reason for the enhanced OER performance of the MG catalyst. To verify this hypothesis, we investigated the structural evolution of the catalyst during long-term acidic OER. As illustrated by the change in surface morphology with reaction time (Fig. 3a), a nanoporous structure gradually developed on the IrTaO_x surface, stabilizing into a bi-continuous nanoporosity with an average size of approximately 100 nm. Even after 400 h, the nanoporous structure remained almost unchanged, indicating its extraordinary stability during the acidic OER catalysis. It should be noted that under the highly acidic and strongly oxidizing conditions of OER, the passivating Ta_2O_5 layer on the surface of IrTaO_x nanostructures is expected to dissolve rapidly and disappear during the initial stages due to its electrochemical corrosion behavior under acidic OER conditions (Fig. S16). Figure 3b, c, respectively, presents the changes in the IrTaO_x layer after 50- and 200-h OER catalysis characterized by TEM. Notably, a unique bi-layer structure emerged during the OER process, characterized by the formation of a thin upper layer with a thickness of approximately 13 nm on top of the IrTaO_x layer. The thickness of this layer remained constant at about 23 nm, exhibiting an obvious nanoporosity after 200 h, consistent with the SEM observation. The HRTEM image of the nanoporous layer (the top right inset in Fig. 3c) reveals the lattice spacing for the (111) plane of IrO_2 , confirming the formation of IrO_2 nanocrystals. This finding is further supported by the STEM elemental mapping analysis of the reacted layer structure (Fig. S17). These characterizations demonstrate that catalytically active nanoporous IrO_2 , with increased accessible contact areas, can be directly self-constructed on IrTaO_x through acidic oxygen evolution, providing abundant active sites for electrocatalytic reactions. Additionally, considerable numbers of nascent IrO_2 nanocrystals were observed to be dispersed within the IrTaO_x layer below (see the right bottom inset in Figs. 3c and S18), indicating further crystallization of the amorphous IrTaO_x layer during the OER process. Moreover, the thickness of the

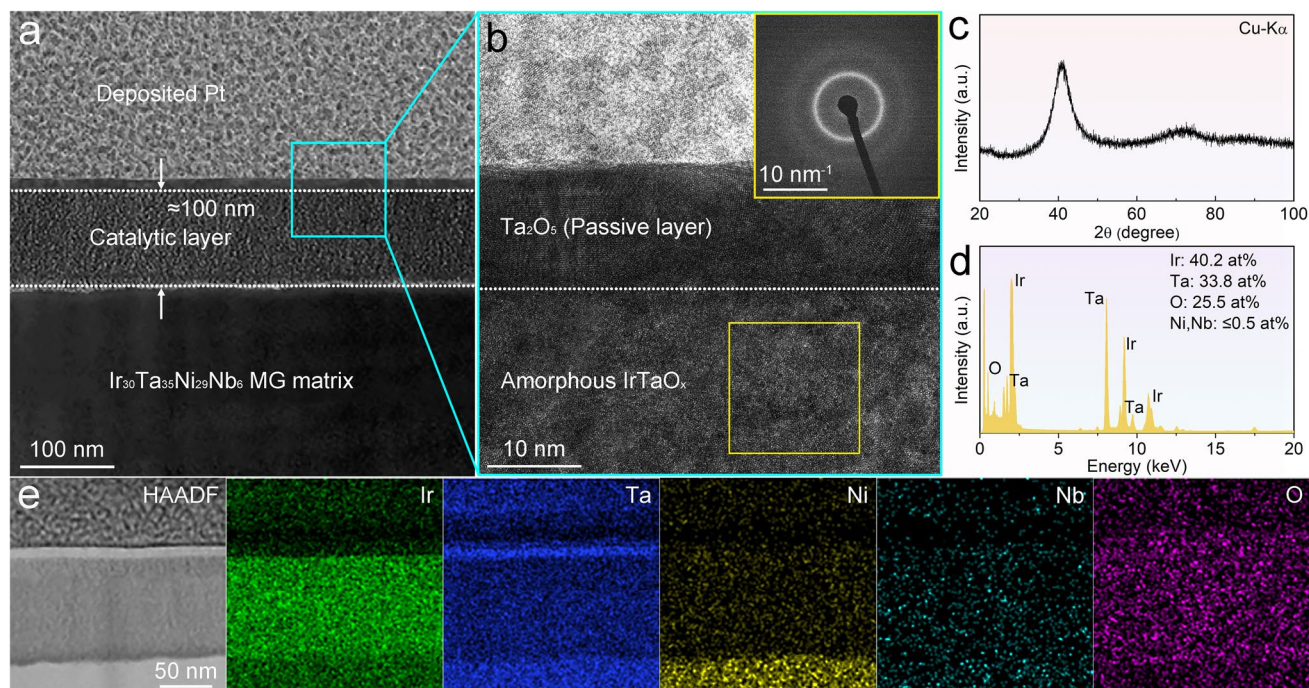


Fig. 2 Characterization of the surface catalytic layer structure. **a** Cross-sectional TEM image of the acid-treated $\text{Ir}_{30}\text{Ta}_{35}\text{Ni}_{29}\text{Nb}_6$ MG (The top layer exhibits the FIB-deposited Pt nanoparticles). **b** HRTEM image of the layer structure marked in **a**. The inset shows the SAED pattern of the region marked by the yellow square. **c** Surface XRD pattern of the IrTaO_x amorphous structure. **d** TEM-EDS analysis of the amorphous IrTaO_x layer. **e** High-angle annular dark-field (HAADF)-STEM image of the layer structure and the corresponding EDS elemental mapping

IrTaO_x layer decreased after long-term OER (i.e., reduced by approximately 24 nm after 200 h), confirming that the surface IrO_2 nanocrystals primarily originate from the underneath IrTaO_x . Given the inevitable dissolution of the surface Ir active species during OER (Fig. S9), it is reasonable to infer that the amorphous IrTaO_x layer acts as a reservoir through inward crystallization and selective dissolution, allowing the newly formed IrO_2 nanocrystals to dynamically compensate for the loss of the surface-active IrO_2 . In this case, the underlying IrTaO_x significantly influences the number of active sites available for electrocatalysis. The increase in the thickness of the IrO_2 nanoporous layer on the catalyst surface is accompanied by a decrease in the thickness of the IrTaO_x layer following prolonged OER. Consequently, the total number of active sites remains relatively stable due to a dynamic replenishment of the underlying IrTaO_x , even as the IrO_2 nanoporous layer continues to thicken. This mechanism provides a replenishment capability that helps maintain the balance of activity and stability on the catalyst surface.

The dynamic evolving process is further illustrated in Fig. 3d, which mainly encompasses the diffusion, oxidation, and dissolution of the constituent elements. Under acidic

and oxidative conditions, the significant accumulation of oxygen atoms on the surface of the metastable amorphous IrTaO_x facilitates the inward diffusion of oxygen. Meanwhile, non-noble Ta elements dissolve outward due to their relatively lower corrosion resistance compared to Ir, resulting in numerous vacancies on the surface. Consequently, Ir atoms tend to diffuse and aggregate to fill these vacancies due to the chemical potential gradient and form IrO_2 by binding with oxygen, thereby resulting in the observed two-layer structure. With continuous oxygen evolution, the amorphous IrTaO_x layer is expected to undergo further crystallization and dynamic evolution, particularly in response to the dissolution of IrO_2 reacted on the surface. Based on these experimental data, it is evident that the self-constructed bi-layer structure on the MG matrix is crucial for enhancing OER performance, where the IrO_2 nanoporous layer generated on the surface provides a high specific surface area that facilitates rapid mass transfer, which contributes to maintaining long-term OER performance. Additionally, the underlying IrTaO_x layer can dynamically evolve into IrO_2 nanocrystals through crystallization and selective dissolution, replenishing the depletion of surface

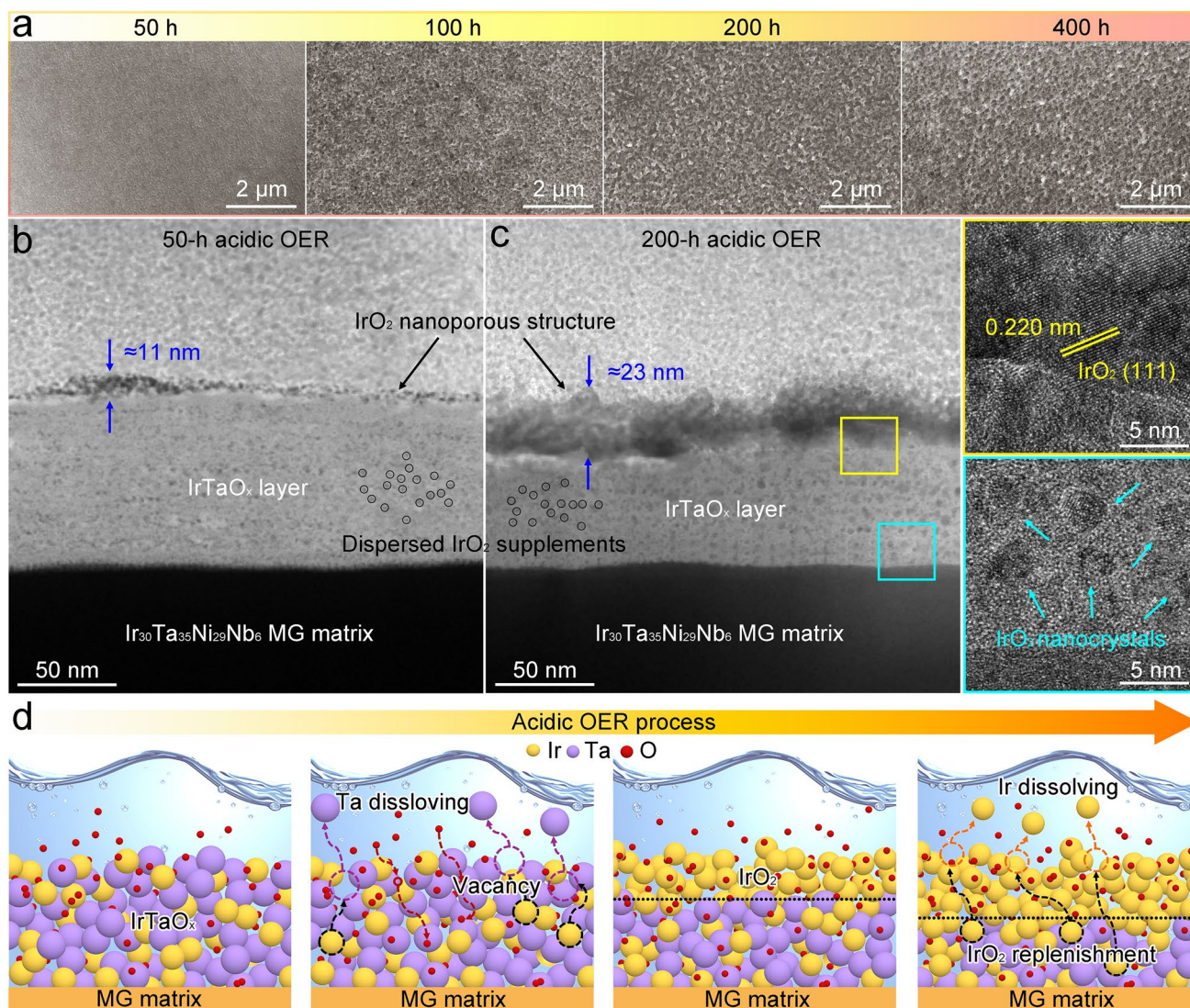


Fig. 3 Dynamical structure evolution during acidic OER. **a** Ex situ surface SEM images for the formation of a nanoporous IrO_2 surface structure under acidic OER conditions. **b** TEM image of the IrTaO_x layer structure after 50-h acidic OER. **c** TEM image of the IrTaO_x layer structure after 200-h acidic OER. The insets show the corresponding HRTEM images of the selected areas marked in **c**. (yellow square: top right; blue square: bottom right). **d** Schematic diagram illustrating the evolution of the IrTaO_x layer structure and the replenishment of surface IrO_2 during OER

Ir active sites and balancing OER activity and stability in acid media.

As is well known, exposed IrO_2 active species play a crucial role in the intrinsic OER property. However, the contribution of the Ta element in the catalyst remains unclear. To understand this, an $\text{Ir}_{30}\text{Ni}_{42}\text{Nb}_{28}$ MG precursor without Ta alloying was prepared for comparison and subjected to the same acid treatment (Figs. S19 and S20). Notably, a nanoporous IrO_2 surface was directly formed on the $\text{Ir}_{30}\text{Ni}_{42}\text{Nb}_{28}$ MG matrix due to the similar corrosion rates of Ni and Nb

(Fig. S21). Compared to the MG catalyst featuring an IrTaO_x surface structure, the acid-treated $\text{Ir}_{30}\text{Ni}_{42}\text{Nb}_{28}$ MG exhibits inferior activity toward acidic OER (Fig. S22). Moreover, during long-term OER operation at 100 mA cm^{-2} , a rapid increase in overpotential was observed in the $\text{Ir}_{30}\text{Ni}_{42}\text{Nb}_{28}$ MG catalyst after only 80 h (Fig. S23). The dissolution of Ir in the electrolyte indicates that its dissolution rate is 30 times higher than that of the $\text{Ir}_{30}\text{Ta}_{35}\text{Ni}_{29}\text{Nb}_6$ MG catalyst (Fig. S24). Furthermore, structural changes observed in the $\text{Ir}_{30}\text{Ni}_{42}\text{Nb}_{28}$ MG catalyst after the stability test suggest that

the surface catalytic sites were depleted, leading to a complete collapse of the catalyst structure after 80 h due to the absence of the IrTaO_x replenishment layer (Fig. S25). The absence of the Ta alloying effect results in the over-oxidative dissolution of surface IrO₂ in strongly acidic and oxidative environments. Additionally, the lack of a dynamic complementary effect from the underlying IrTaO_x structure leads to the formation of numerous vacancies and defects on the catalyst surface, increasing susceptibility to localized corrosion. Stress concentration in the corroded areas serves as a source for crack initiation, ultimately resulting in localized spallation fractures of the catalyst surface [54]. As IrO₂ dissolves and detaches from the catalyst surface, the oxidation rate of the MG matrix accelerates, leading to the collapse of the overall structure and a decline in OER performance. The EDS results for the Ir₃₀Ni₄₂Nb₂₈ MG catalyst after the stability test indicate a decrease in the atomic ratio of the Ir element, with the catalyst becoming completely oxidized (Table S4). Moreover, we also evaluated the stability of the acid-treated Ir₆₅Ni₂₉Nb₆, which has a higher Ir content (Fig. S26). During the 50-h OER test, the catalyst's voltage increased, indicating a decline in catalytic performance. The deep purple color of the electrolyte after 50 h of OER further suggests that Ir is rapidly dissolving due to peroxidation in the absence of Ta. These results clearly demonstrate that the Ta element is essential for the formation of the IrO₂/IrTaO_x bi-layer structure and plays a significant role in enhancing stability during acidic OER.

3.3 Electronic Structure Analysis and Reaction Mechanism

Given the critical role of Ta alloying in affecting OER performance, it is essential to further evaluate its electronic interaction with Ir during OER [55–57]. The surface chemical state of the catalyst was examined using high-resolution XPS. Figure 4a illustrates the variation in the Ir 4f spectra on the MG catalyst surface during the OER process from 0 to 200 h. After 50 h, the metallic Ir was completely transformed into oxides compared to its initial state. Specifically, the oxidation states of Ir can be attributed to the Ir^{IV} and Ir^{III} species, which are located at 62.1/65.1 and 63.0/65.8 eV, respectively. It should also be noted that due to anodic polarization, the binding energy of Ir shifts positively by 0.2 to 0.3 eV after 100 h of OER, which may facilitate the further conversion of Ir^{III} to Ir^{IV}.

As the reaction progressed to 200 h, significant changes were observed in the peak areas of the Ir^{IV} and Ir^{III} species, with Ir^{III} completely converted into Ir^{IV}. Moreover, the Ir 4f spectra reveal a counterintuitive decrease in the binding energy of Ir^{IV} by approximately 0.2 to 0.3 eV, indicating that the formed Ir^{IV} species are stable and would not be over-oxidized to higher oxidation states (i.e., Ir^V and Ir^{VI}). In fact, recent studies have demonstrated that the pathways for the OER-triggered dissolution of Ir primarily involve the formation of soluble Ir^{III} or hypervalent Ir (> IV) species [58, 59]. Therefore, the surface-stabilized Ir^{IV} species in our case should account for the high chemical stability. We also characterized the variations in the Ta 4f spectra. As shown in Fig. 4b, the difference in XPS peaks reveals the complete transformation of the metallic Ta⁰ to oxidized Ta^V during the acidic OER. Additionally, the binding energy of Ta^V exhibits a positive shift of approximately 0.6 to 0.7 eV relative to its initial state, indicating the electronic modulation of Ir by Ta during OER. The high valence oxidation of Ta caused by the strong electronic interactions between Ir and Ta can adsorb excess oxygen atoms and prevent active Ir oxides from further oxidizing to higher valence states (e.g., the unstable Ir^V or Ir^{VI} species) during acidic OER, thereby enhancing the durability of the catalyst.

Figure 4c further illustrates the variation in the O 1s XPS spectra during the acidic OER process. The core-level spectra can be deconvoluted into three distinct oxygen species: adsorbed H₂O, adsorbed OH, and lattice oxygen. Furthermore, to differentiate the lattice oxygen bound to various metals, the species at 531.0 eV were identified as Ta–O, while the peak near 530.1 eV is attributed to Ir–O [60, 61]. In this context, Ta atoms, which possess lower electronegativity, are expected to preferentially bind with oxygen intermediates, thereby minimizing electron loss of Ir and inhibiting the further oxidation of the surface-active Ir oxides to soluble high-valence counterparts. Additionally, it was observed that the area ratio of lattice oxygen to adsorbed OH on the catalyst surface increased after prolonged OER testing. This trend indicates that the surface-adsorbed oxygen is less susceptible to protonation and is more likely to react with H₂O in the electrolyte to form hydroperoxide intermediates and then produce O₂, indicating a preference for the adsorbate evolution mechanism (AEM) over the lattice oxygen mechanism (LOM) [62]. To experimentally validate this AEM pathway, isotope-labeled operando DEMS measurements were conducted (see the schematic diagram in the inset of Fig. 4d). Initially, the catalyst surface was labeled with ¹⁸O by conducting

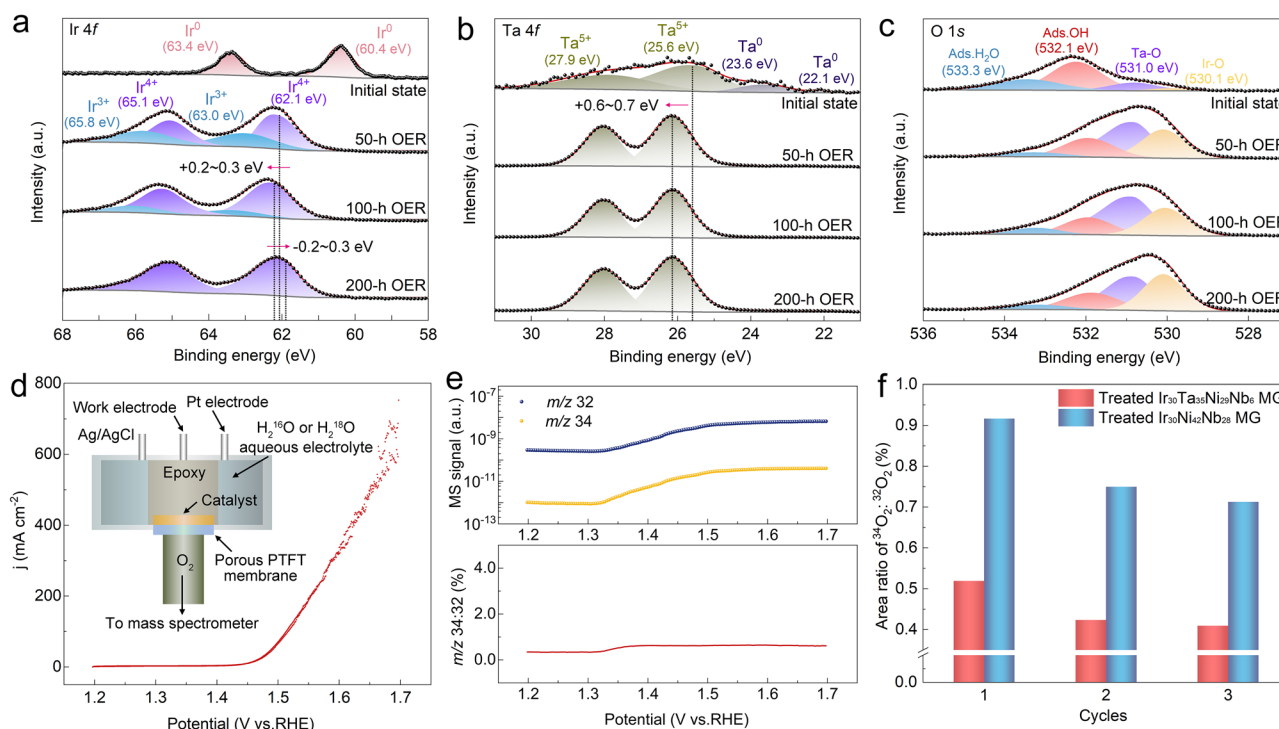


Fig. 4 XPS analysis and isotope-labeled operando DEMS characterization. **a–c** XPS spectra of **a** Ir 4f, **b** Ta 4f, and **c** O 1s during the long-term acidic OER stability test (at 0, 50, 100, and 200 h). **d** CV cycle of the MG catalyst measured by DEMS. The inset shows the schematic illustration of the operando DEMS. **e** Top: DEMS signals of $^{32}\text{O}_2$ ($^{16}\text{O} + ^{16}\text{O}$) and $^{34}\text{O}_2$ ($^{16}\text{O} + ^{18}\text{O}$) collected during CV cycle; Bottom: The mass spectroscopy peak area ratio of $^{34}\text{O}_2/^{32}\text{O}_2$ with increase in potential. **f** The ratio of $^{34}\text{O}_2/^{32}\text{O}_2$ for the $\text{Ir}_{30}\text{Ta}_{35}\text{Ni}_{29}\text{Nb}_6$ and $\text{Ir}_{30}\text{Ni}_{42}\text{Nb}_{28}$ MG catalysts in $\text{H}_2^{16}\text{O}/0.5\text{ M H}_2\text{SO}_4$ electrolyte during 3 OER cycles

OER under a constant current density in an $\text{H}_2^{18}\text{O}/0.5\text{ M H}_2\text{SO}_4$ electrolyte. Then, the ^{18}O -labeled MG catalyst was thoroughly washed with H_2^{16}O to eliminate any adsorbed H_2^{18}O , followed by OER cycles in an $\text{H}_2^{16}\text{O}/0.5\text{ M H}_2\text{SO}_4$ electrolyte (Fig. 4d). As the OER current increased, gaseous oxygen products including $^{32}\text{O}_2$ ($^{16}\text{O}^{16}\text{O}$), $^{34}\text{O}_2$ ($^{16}\text{O}^{18}\text{O}$), and $^{36}\text{O}_2$ ($^{18}\text{O}^{18}\text{O}$) were detected by online mass spectroscopy (Fig. 4e). It is worth noting that the signal ratio of $^{34}\text{O}_2$ to $^{32}\text{O}_2$ within the OER potential range remained nearly constant at a low value of approximately 0.53%, indicating that the LOM pathway did not significantly occur on the catalyst surface. Moreover, it is important to highlight that the value of $^{34}\text{O}_2/^{32}\text{O}_2$ generated on the MG catalyst is much lower than that of the reference MG without Ta alloying (i.e., the $\text{Ir}_{30}\text{Ni}_{42}\text{Nb}_{28}$ MG catalyst) (Figs. 4f and S27), suggesting an inhibitory effect of lattice oxygen participation on the $\text{IrO}_2/\text{IrTaO}_x$ catalytic surface. The aforementioned DEMS results demonstrate that the incorporation of Ta effectively inhibits the participation of lattice oxygen during acidic OER, thereby stabilizing the surface IrO_2 and enhancing stability.

We then performed DFT calculations to gain deeper insight into the impact of Ta electronic modulation on catalyst stability. For the convenience of this analysis, a simplified $(\text{Ir}, \text{Ta})\text{O}_2$ structure was modeled to simulate the catalytic surface based on the TEM-EDS result and surface ICP analysis (Table S3). Subsequently, the model was compared to the pristine IrO_2 crystal (Fig. S28). Figure 5a illustrates the charge density distribution of the (110) crystal plane for both $(\text{Ir}, \text{Ta})\text{O}_2$ and IrO_2 , demonstrating that Ta atoms act as electron donors. The corresponding Bader charge distribution further indicates that, after Ta alloying, the donating electrons of Ir decrease from -1.601 to -1.375 e , while the accepting electrons of O increase from 0.799 to 1.121 e (Fig. 5b and Tables S5 and S6). This observation suggests that the valence state of the Ir cations decreases with the addition of Ta, potentially enhancing the resistance of Ir to dissolution in acid environments. Furthermore, the reduction in covalency for Ir–O resulted in the formation of additional Ta–O bonds. The strong electronic interaction in the resulting Ir–O–Ta local structure contributes to the formation of

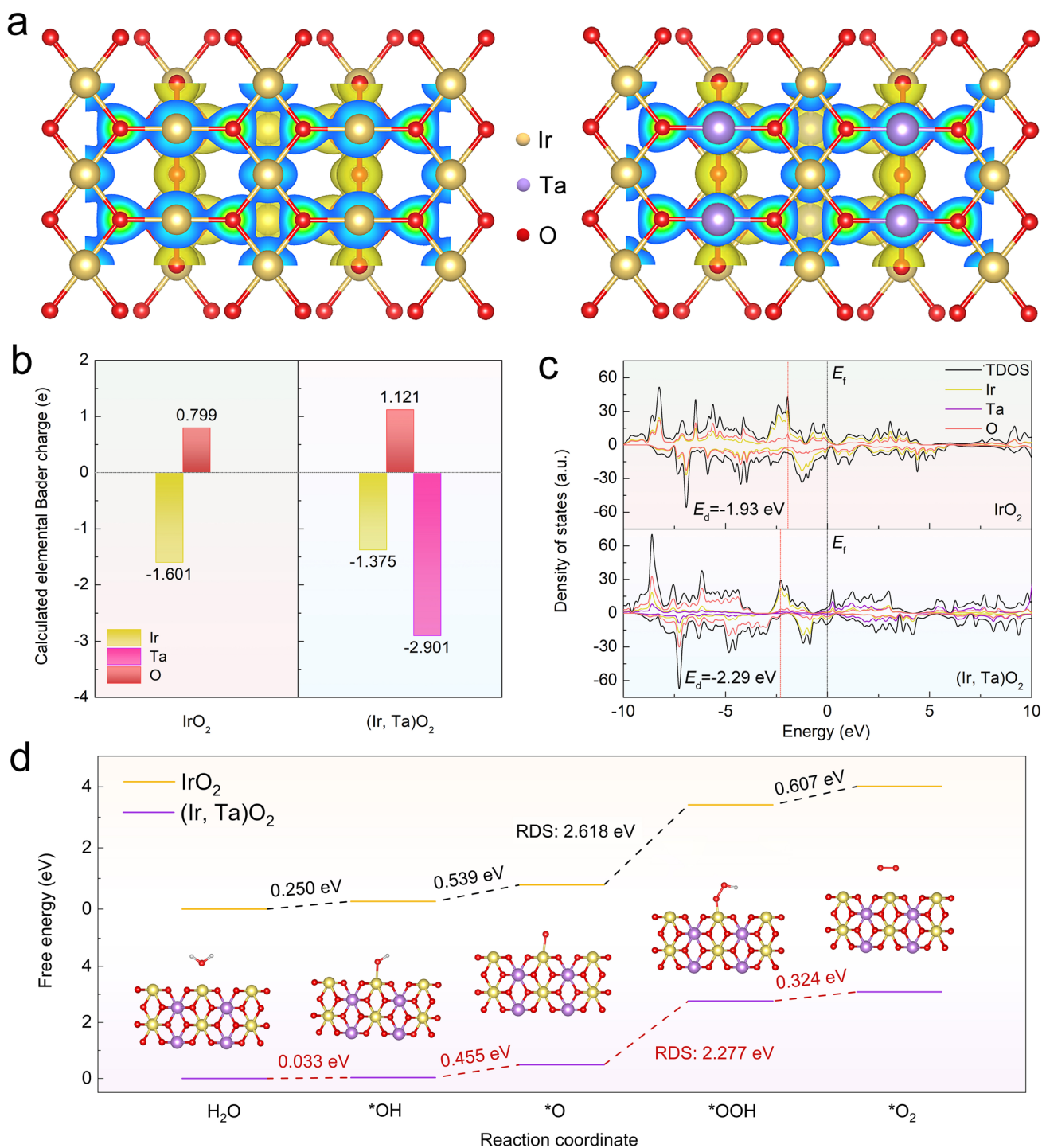


Fig. 5 DFT calculation. **a** Charge density distribution of the (110) crystal plane for (Ir, Ta)O₂ and IrO₂ models. **b** Bader charges distribution of the modulated IrO₂ and (Ir, Ta)O₂ structure. **c** Calculated PDOS of IrO₂ and (Ir, Ta)O₂. E_f represents the Fermi energy level and E_d represents the d-band center. **d** OER free energy diagram for (Ir, Ta)O₂ and IrO₂ at a zero applied potential

a more stable surface configuration, which may further suppress the involvement of lattice oxygen during OER, thereby improving catalyst stability [63]. Figure 5c depicts the

projected density of states (PDOS) of the simulated structures of (Ir, Ta)O₂ and IrO₂. The introduction of Ta leads to an increase in the total density of states near the Fermi

energy level, indicating that Ta atoms can effectively modulate the *d*-electron characteristics of Ir, thereby optimizing the local coordination of reactive Ir sites. Additionally, it was observed that the energy levels of the orbitals for Ta and O atoms gradually raised, with the strongest hybridization occurring near the Fermi energy level. This observation further supports the preferential formation of Ta-O bonds. Moreover, a downward shift in the *d*-band center is noted for (Ir, Ta)O₂ (− 2.29 eV) compared to IrO₂ (− 1.93 eV), which can effectively weaken the adsorption strength of O-based intermediates, thereby enhancing the catalytic efficiency during the acidic OER process [64]. We also calculated the OER free energy diagrams of IrO₂ and (Ir, Ta)O₂ at a zero applied potential of U = 0 V (standard potential). The overall OER reaction pathway in acidic media mainly follows the AEM, involving four concerted proton–electron pairs transfer. The rate-determining step (RDS) is identified as the conversion from *O to *OOH for both (Ir, Ta)O₂ and IrO₂ (Fig. 5d). The relative energy barrier of the (Ir, Ta)O₂ model is reduced to 2.277 eV, significantly lower than that of IrO₂ (2.618 eV), suggesting that Ir sites in (Ir, Ta)O₂ are efficient active sites to greatly promote reaction kinetics of water oxidation. This enhancement can be primarily attributed to the electronic synergistic effect between Ir and Ta, which optimizes the adsorption strengths of the O-based intermediates by downshifting the *d*-band center, thereby modulating the adsorption energies of the OER intermediates.

4 Conclusion

In summary, we have developed a unique IrO₂/IrTaO_x bi-layer nanostructure for acidic OER by using a specially designed Ir-Ta-Ni-Nb MG as the matrix. During the OER process, the nanoporous IrO₂ surface with high catalytic activity was formed in situ on the amorphous IrTaO_x, which provides more accessible active sites and enhances electron transfer. Furthermore, the IrTaO_x nanostructure beneath can dynamically evolve into IrO₂ nanocrystals through inward crystallization and dissolution, efficiently replenishing the depletion of surface-active sites. As a result, the self-constructed bi-layered catalyst exhibits a high mass activity of 1.06 A mg_{Ir}^{−1} at a 300 mV overpotential and delivers more than 650 h of long-term OER stability under a current density of 100 mA cm^{−2}. Electronic structure analyses,

combined with DEMS measurements, reveal that the strong electronic interaction between Ir and Ta can balance the valence state of active Ir species, which prevents the formation of hypervalent soluble species and suppresses the involvement of lattice oxygen during OER, thereby further enhancing the catalytic stability. This work provides new insight into the stabilization of active Ir oxides for long-term acidic OER and opens a new avenue for the development of efficient and durable catalysts for practical PEM water electrolysis applications.

Acknowledgements This work was financially supported by the National Natural Science Foundation of China (Nos. 52101202, 52071024), the Funds for Creative Research Groups of China (No. 51921001), the National Key Research and Development Program of China (No. 2022YFB3707103), the Gusu Leading Talents Program (No. ZXL2021206), the Basic Research Program of Taicang (No. TC2023JC29), the Fundamental Research Fund for the Central Universities of China, GuangDong Basic and Applied Basic Research Foundation, and State Key Lab for Advanced Metals and Materials (No. 2024-Z11).

Authors' Contribution QG performed most of the experiments and wrote the paper. YNZ, QQZ, YH, and ZBL supported the experiments on material fabrication and structural analysis. WHL assisted in the analysis of TEM results and reviewed the paper. RL, XJL, and ZPL conceived the idea, reviewed the manuscript, and provided financial support. All authors discussed the results and commented on the manuscript.

Declarations

Conflict of Interest The authors declare no conflict of interest. They have no known competing financial interests or personal relationships that could have appeared to influence the work reported in this paper.

Open Access This article is licensed under a Creative Commons Attribution 4.0 International License, which permits use, sharing, adaptation, distribution and reproduction in any medium or format, as long as you give appropriate credit to the original author(s) and the source, provide a link to the Creative Commons licence, and indicate if changes were made. The images or other third party material in this article are included in the article's Creative Commons licence, unless indicated otherwise in a credit line to the material. If material is not included in the article's Creative Commons licence and your intended use is not permitted by statutory regulation or exceeds the permitted use, you will need to obtain permission directly from the copyright holder. To view a copy of this licence, visit <http://creativecommons.org/licenses/by/4.0/>.

Supplementary Information The online version contains supplementary material available at <https://doi.org/10.1007/s40820-025-01680-w>.

References

1. J.A. Turner, Sustainable hydrogen production. *Science* **305**, 972–974 (2004). <https://doi.org/10.1126/science.1103197>
2. S. Chu, A. Majumdar, Opportunities and challenges for a sustainable energy future. *Nature* **488**, 294–303 (2012). <https://doi.org/10.1038/nature11475>
3. M. Carmo, G.P. Keeley, D. Holtz, T. Grube, M. Robinius et al., PEM water electrolysis: innovative approaches towards catalyst separation, recovery and recycling. *Int. J. Hydrog. Energy* **44**, 3450–3455 (2019). <https://doi.org/10.1016/j.ijhydene.2018.12.030>
4. S.Z. Oener, M.J. Foster, S.W. Boettcher, Accelerating water dissociation in bipolar membranes and for electrocatalysis. *Science* **369**, 1099–1103 (2020). <https://doi.org/10.1126/science.aaz1487>
5. R. Haider, Y. Wen, Z.-F. Ma, D.P. Wilkinson, L. Zhang et al., High temperature proton exchange membrane fuel cells: progress in advanced materials and key technologies. *Chem. Soc. Rev.* **50**, 1138–1187 (2021). <https://doi.org/10.1039/D0CS00296H>
6. K. Jiao, J. Xuan, Q. Du, Z. Bao, B. Xie et al., Designing the next generation of proton-exchange membrane fuel cells. *Nature* **595**, 361–369 (2021). <https://doi.org/10.1038/s41586-021-03482-7>
7. X. Li, L. Zhao, J. Yu, X. Liu, X. Zhang et al., Water splitting: from electrode to green energy system. *Nano-Micro Lett.* **12**, 131 (2020). <https://doi.org/10.1007/s40820-020-00469-3>
8. H. Jin, B. Ruqia, Y. Park, H.J. Kim, H.-S. Oh et al., Nanocatalyst design for long-term operation of proton/anion exchange membrane water electrolysis. *Adv. Energy Mater.* **11**, 2003188 (2021). <https://doi.org/10.1002/aenm.202003188>
9. H. Wang, Z.-N. Chen, D. Wu, M. Cao, F. Sun et al., Significantly enhanced overall water splitting performance by partial oxidation of Ir through Au modification in core-shell alloy structure. *J. Am. Chem. Soc.* **143**, 4639–4645 (2021). <https://doi.org/10.1021/jacs.0c12740>
10. F. Xiao, Y.-C. Wang, Z.-P. Wu, G. Chen, F. Yang et al., Recent advances in electrocatalysts for proton exchange membrane fuel cells and alkaline membrane fuel cells. *Adv. Mater.* **33**, 2006292 (2021). <https://doi.org/10.1002/adma.202006292>
11. L. Li, P. Wang, Q. Shao, X. Huang, Recent progress in advanced electrocatalyst design for acidic oxygen evolution reaction. *Adv. Mater.* **33**, e2004243 (2021). <https://doi.org/10.1002/adma.202004243>
12. F.-Y. Chen, Z.-Y. Wu, Z. Adler, H. Wang, Stability challenges of electrocatalytic oxygen evolution reaction: from mechanistic understanding to reactor design. *Joule* **5**, 1704–1731 (2021). <https://doi.org/10.1016/j.joule.2021.05.005>
13. C. Spöri, J.T.H. Kwan, A. Bonakdarpour, D.P. Wilkinson, P. Strasser, The stability challenges of oxygen evolving catalysts: towards a common fundamental understanding and mitigation of catalyst degradation. *Angew. Chem. Int. Ed.* **56**, 5994–6021 (2017). <https://doi.org/10.1002/anie.201608601>
14. R. Qin, G. Chen, X. Feng, J. Weng, Y. Han, Ru/Ir-based electrocatalysts for oxygen evolution reaction in acidic conditions: from mechanisms, optimizations to challenges. *Adv. Sci.* **11**, e2309364 (2024). <https://doi.org/10.1002/advs.202309364>
15. A. Lončar, D. Escalera-López, S. Cherevko, N. Hodnik, Interrelationships between oxygen evolution and iridium dissolution mechanisms. *Angew. Chem. Int. Ed.* **61**, e202114437 (2022). <https://doi.org/10.1002/anie.202114437>
16. L.C. Seitz, C.F. Dickens, K. Nishio, Y. Hikita, J. Montoya et al., A highly active and stable IrO_x/SrIrO₃ catalyst for the oxygen evolution reaction. *Science* **353**, 1011–1014 (2016). <https://doi.org/10.1126/science.aaf5050>
17. R. Li, H. Wang, F. Hu, K.C. Chan, X. Liu et al., IrW nanochannel support enabling ultrastable electrocatalytic oxygen evolution at 2 A cm⁻² in acidic media. *Nat. Commun.* **12**, 3540 (2021). <https://doi.org/10.1038/s41467-021-23907-1>
18. J. Zhang, X. Fu, F. Xia, W. Zhang, D. Ma et al., Core-shell nanostructured Ru@Ir-O electrocatalysts for superb oxygen evolution in acid. *Small* **18**, e2108031 (2022). <https://doi.org/10.1002/sml.202108031>
19. Y. Chen, H. Li, J. Wang, Y. Du, S. Xi et al., Exceptionally active iridium evolved from a pseudo-cubic perovskite for oxygen evolution in acid. *Nat. Commun.* **10**, 572 (2019). <https://doi.org/10.1038/s41467-019-08532-3>
20. W.H. Lee, J. Yi, H.N. Nong, P. Strasser, K.H. Chae et al., Electroactivation-induced IrNi nanoparticles under different pH conditions for neutral water oxidation. *Nanoscale* **12**, 14903–14910 (2020). <https://doi.org/10.1039/d0nr02951c>
21. L. Fu, X. Zeng, G. Cheng, W. Luo, IrCo nanodendrite as an efficient bifunctional electrocatalyst for overall water splitting under acidic conditions. *ACS Appl. Mater. Interfaces* **10**, 24993–24998 (2018). <https://doi.org/10.1021/acsami.8b08717>
22. L. An, C. Wei, M. Lu, H. Liu, Y. Chen et al., Recent development of oxygen evolution electrocatalysts in acidic environment. *Adv. Mater.* **33**, 2006328 (2021). <https://doi.org/10.1002/adma.202006328>
23. Y.-R. Zheng, J. Vernieres, Z. Wang, K. Zhang, D. Hochfilzer et al., Monitoring oxygen production on mass-selected iridium–tantalum oxide electrocatalysts. *Nat. Energy* **7**, 55–64 (2022). <https://doi.org/10.1038/s41560-021-00948-w>
24. S. Hao, H. Sheng, M. Liu, J. Huang, G. Zheng et al., Torsion strained iridium oxide for efficient acidic water oxidation in proton exchange membrane electrolyzers. *Nat. Nanotechnol.* **16**, 1371–1377 (2021). <https://doi.org/10.1038/s41565-021-00986-1>
25. Z. Lu, C. Wei, X. Liu, Y. Fang, X. Hao et al., Regulating the adsorption behavior of intermediates on Ir–W@Ir–WO_{3-x} boosts acidic water oxidation electrocatalysis. *Mater. Chem. Front.* **5**, 6092–6100 (2021). <https://doi.org/10.1039/d1qm00551k>
26. Z. Shi, J. Li, J. Jiang, Y. Wang, X. Wang et al., Enhanced acidic water oxidation by dynamic migration of oxygen species at the Ir/Nb₂O_{5-x} catalyst/support interfaces. *Angew. Chem. Int. Ed.* **61**, e202212341 (2022). <https://doi.org/10.1002/anie.202212341>



27. A.A.H. Tajuddin, M. Wakisaka, T. Ohto, Y. Yu, H. Fukushima et al., Corrosion-resistant and high-entropic non-noble-metal electrodes for oxygen evolution in acidic media. *Adv. Mater.* **35**, e2207466 (2023). <https://doi.org/10.1002/adma.202207466>
28. H. Zhu, Z. Zhu, J. Hao, S. Sun, S. Lu et al., High-entropy alloy stabilized active Ir for highly efficient acidic oxygen evolution. *Chem. Eng. J.* **431**, 133251 (2022). <https://doi.org/10.1016/j.cej.2021.133251>
29. S. Niu, Z. Yang, F. Qi, Y. Han, Z. Shi et al., Electrical discharge induced bulk-to-nanoparticle transformation: nano high-entropy carbide as catalysts for hydrogen evolution reaction. *Adv. Funct. Mater.* **32**, 2203787 (2022). <https://doi.org/10.1002/adfm.202203787>
30. O. Kasian, J.-P. Grote, S. Geiger, S. Cherevko, K.J.J. Mayrhofer, The common intermediates of oxygen evolution and dissolution reactions during water electrolysis on iridium. *Angew. Chem. Int. Ed.* **57**, 2488–2491 (2018). <https://doi.org/10.1002/anie.201709652>
31. Y.T. Kim, P.P. Lopes, S.A. Park, A.Y. Lee, J. Lim et al., Balancing activity, stability and conductivity of nanoporous core-shell iridium/iridium oxide oxygen evolution catalysts. *Nat. Commun.* **8**, 1449 (2017). <https://doi.org/10.1038/s41467-017-01734-7>
32. S. Geiger, O. Kasian, B.R. Shrestha, A.M. Mingers, K.J.J. Mayrhofer et al., Activity and stability of electrochemically and thermally treated iridium for the oxygen evolution reaction. *J. Electrochem. Soc.* **163**, F3132–F3138 (2016). <https://doi.org/10.1149/2.0181611jes>
33. T.R. Hellstern, J.D. Benck, J. Kibsgaard, C. Hahn, T.F. Jaramillo, Engineering cobalt phosphide (CoP) thin film catalysts for enhanced hydrogen evolution activity on silicon photocathodes. *Adv. Energy Mater.* **6**, 1501758 (2016). <https://doi.org/10.1002/aenm.201501758>
34. Y. Hao, S.-F. Hung, W.-J. Zeng, Y. Wang, C. Zhang et al., Switching the oxygen evolution mechanism on atomically dispersed Ru for enhanced acidic reaction kinetics. *J. Am. Chem. Soc.* **145**, 23659–23669 (2023). <https://doi.org/10.1021/jacs.3c07777>
35. G. Kresse, J. Furthmüller, Efficient iterative schemes for ab initio total-energy calculations using a plane-wave basis set. *Phys. Rev. B Condens. Matter* **54**, 11169–11186 (1996). <https://doi.org/10.1103/physrevb.54.11169>
36. G. Kresse, D. Joubert, From ultrasoft pseudopotentials to the projector augmented-wave method. *Phys. Rev. B* **59**, 1758–1775 (1999). <https://doi.org/10.1103/physrevb.59.1758>
37. G. Kresse, J. Hafner, Ab initio molecular dynamics for liquid metals. *Phys. Rev. B Condens. Matter* **47**, 558–561 (1993). <https://doi.org/10.1103/physrevb.47.558>
38. J.P. Perdew, K. Burke, M. Ernzerhof, Generalized gradient approximation made simple. *Phys. Rev. Lett.* **77**, 3865–3868 (1996). <https://doi.org/10.1103/physrevlett.77.3865>
39. P.E. Blöchl, Projector augmented-wave method. *Phys. Rev. B Condens. Matter* **50**, 17953–17979 (1994). <https://doi.org/10.1103/physrevb.50.17953>
40. S. Niu, S. Li, Y. Du, X. Han, P. Xu, How to reliably report the overpotential of an electrocatalyst. *ACS Energy Lett.* **5**, 1083–1087 (2020). <https://doi.org/10.1021/acscenergylett.0c00321>
41. S. Anantharaj, P.E. Karthik, S. Noda, The significance of properly reporting turnover frequency in electrocatalysis research. *Angew. Chem. Int. Ed.* **60**, 23051–23067 (2021). <https://doi.org/10.1002/anie.202110352>
42. S. Geiger, O. Kasian, M. Ledendecker, E. Pizzutilo, A.M. Mingers et al., The stability number as a metric for electrocatalyst stability benchmarking. *Nat. Catal.* **1**, 508–515 (2018). <https://doi.org/10.1038/s41929-018-0085-6>
43. C. Van Pham, M. Bühler, J. Knöppel, M. Bierling, D. Seiberger et al., IrO₂ coated TiO₂ core-shell microparticles advance performance of low loading proton exchange membrane water electrolyzers. *Appl. Catal. B Environ.* **269**, 118762 (2020). <https://doi.org/10.1016/j.apcatb.2020.118762>
44. L. Yang, K. Zhang, H. Chen, L. Shi, X. Liang et al., An ultrathin two-dimensional iridium-based perovskite oxide electrocatalyst with highly efficient {001} facets for acidic water oxidation. *J. Energy Chem.* **66**, 619–627 (2022). <https://doi.org/10.1016/j.jechem.2021.09.016>
45. R. Zhang, N. Dubouis, M. BenOsman, W. Yin, M.T. Sougrati et al., A dissolution/precipitation equilibrium on the surface of iridium-based perovskites controls their activity as oxygen evolution reaction catalysts in acidic media. *Angew. Chem. Int. Ed.* **58**, 4571–4575 (2019). <https://doi.org/10.1002/anie.201814075>
46. J. Edgington, R. Vicente, S. Vispute, R. Li, M.E. Sweers et al., Dynamics of highly active Ln₃IrO₇ catalysts for the oxygen evolution reaction in acid. *Adv. Energy Mater.* **14**, 2402333 (2024). <https://doi.org/10.1002/aenm.202402333>
47. Z. Xie, H. Chen, X. Wang, Y.A. Wu, Z. Wang et al., Honeycomb-structured IrO_x foam platelets as the building block of anode catalyst layer in PEM water electrolyzer. *Angew. Chem. Int. Ed.* **64**, e202415032 (2025). <https://doi.org/10.1002/anie.202415032>
48. Y. Xu, Z. Mao, J. Zhang, J. Ji, Y. Zou et al., Strain-modulated Ru–O covalency in Ru–Sn oxide enabling efficient and stable water oxidation in acidic solution. *Angew. Chem. Int. Ed.* **63**, e202316029 (2024). <https://doi.org/10.1002/anie.202316029>
49. G. Yu, R. Li, Y. Zhang, X. Lin, G. Wang et al., Constructing high coordination number of Ir–O–Ru bonds in IrRuO₆ nanomeshes for highly stable acidic oxygen evolution reaction. *Nano Res.* **17**, 5073–5079 (2024). <https://doi.org/10.1007/s12274-024-6524-6>
50. H. Dai, S. Shi, L. Yang, C. Guo, X. Chen, Recent progress on the corrosion behavior of metallic materials in HF solution. *Corros. Rev.* **39**, 313–337 (2021). <https://doi.org/10.1515/corrrev-2020-0101>
51. W.-Q. Chen, S.-M. Zhang, J. Qiu, Surface analysis and corrosion behavior of pure titanium under fluoride exposure. *J. Prosthet. Dent.* **124**(239), e1-239239.e8 (2020). <https://doi.org/10.1016/j.prosdent.2020.02.022>

52. A. Kocijan, D.K. Merl, M. Jenko, The corrosion behaviour of austenitic and duplex stainless steels in artificial saliva with the addition of fluoride. *Corros. Sci.* **53**, 776–783 (2011). <https://doi.org/10.1016/j.corsci.2010.11.010>
53. M.C. Li, C.L. Zeng, H.C. Lin, C.N. Cao, Electrochemical corrosion behaviour of type 316 stainless steel in acid media containing fluoride ions. *Br. Corros. J.* **36**, 179–183 (2001). <https://doi.org/10.1179/bcj.2001.36.3.179>
54. H. Li, Y. Liu, S. Pang, P.K. Liaw, T. Zhang, Corrosion fatigue behavior of a Mg-based bulk metallic glass in a simulated physiological environment. *Intermetallics* **73**, 31–39 (2016). <https://doi.org/10.1016/j.intermet.2016.03.003>
55. C. Han, T. Wang, Understanding the catalytic performances of metal-doped Ta₂O₅ catalysts for acidic oxygen evolution reaction with computations. *Chem. Sci.* **15**, 14371–14378 (2024). <https://doi.org/10.1039/d4sc03554b>
56. C. Baik, J. Cho, J.I. Cha, Y. Cho, S.S. Jang et al., Electron-rich Ir nanostructure supported on mesoporous Ta₂O₅ for enhanced activity and stability of oxygen evolution reaction. *J. Power Sources* **575**, 233174 (2023). <https://doi.org/10.1016/j.jpowsour.2023.233174>
57. J.S. Dondapati, A.R. Thirupathi, A. Salverda, A. Chen, Comparison of Pt and IrO₂-Ta₂O₅/Ti as a counter electrode in acidic media. *Electrochem. Commun.* **124**, 106946 (2021). <https://doi.org/10.1016/j.elecom.2021.106946>
58. T. Reier, H.N. Nong, D. Teschner, R. Schlögl, P. Strasser, Electrocatalytic oxygen evolution reaction in acidic environments—reaction mechanisms and catalysts. *Adv. Energy Mater.* **7**, 1601275 (2017). <https://doi.org/10.1002/aenm.201601275>
59. A. Minguzzi, O. Lugaresi, E. Achilli, C. Locatelli, A. Vertova et al., Observing the oxidation state turnover in heterogeneous iridium-based water oxidation catalysts. *Chem. Sci.* **5**, 3591–3597 (2014). <https://doi.org/10.1039/C4SC00975D>
60. T. Reier, Z. Pawolek, S. Cherevko, M. Bruns, T. Jones et al., Molecular insight in structure and activity of highly efficient, low-Ir Ir-Ni oxide catalysts for electrochemical water splitting (OER). *J. Am. Chem. Soc.* **137**, 13031–13040 (2015). <https://doi.org/10.1021/jacs.5b07788>
61. E. Atanassova, G. Tyuliev, A. Paskaleva, D. Spassov, K. Kostov, XPS study of N₂ annealing effect on thermal Ta₂O₅ layers on Si. *Appl. Surf. Sci.* **225**, 86–99 (2004). <https://doi.org/10.1016/j.apsusc.2003.09.040>
62. Y. Wen, P. Chen, L. Wang, S. Li, Z. Wang et al., Stabilizing highly active Ru sites by suppressing lattice oxygen participation in acidic water oxidation. *J. Am. Chem. Soc.* **143**, 6482–6490 (2021). <https://doi.org/10.1021/jacs.1c00384>
63. Y. Qin, T. Yu, S. Deng, X.-Y. Zhou, D. Lin et al., RuO₂ electronic structure and lattice strain dual engineering for enhanced acidic oxygen evolution reaction performance. *Nat. Commun.* **13**, 3784 (2022). <https://doi.org/10.1038/s41467-022-31468-0>
64. R. Liu, C. Wang, Y. Yan, R. Wang, G. Chen, Reversed charge transfer to modulate the d-band center of Pd for efficient direct H₂O₂ synthesis. *ACS Catal.* **14**, 3955–3965 (2024). <https://doi.org/10.1021/acscatal.3c05910>

Publisher's Note Springer Nature remains neutral with regard to jurisdictional claims in published maps and institutional affiliations.

